Journal of ELECTRONIC MATERIALS, Vol. 49, No. 3, 2020
https://doi.org/10.1007/s11664-020-07943-z

PROGRESS AND CHALLENGES IN DEVELOPING ELECTROMAGNETIC INTERFERENCE MATERIALS

Effects of Calcination Temperature on Magnetic and Microwave Absorption Properties of $SrFe_{12}O_{19}/Ni_{0.6}Zn_{0.4}Fe_2O_4$ Composites

S.R. SAEEDI AFSHAR,[1] S.M. MASOUDPANAH,[1]
and M. HASHEMINIASARI[1,2]

1.—School of Metallurgy and Materials Engineering, Iran University of Science and Technology (IUST), Tehran, Iran. 2.—e-mail: mhashemi@iust.ac.ir

$SrFe_{12}O_{19}/Ni_{0.6}Zn_{0.4}Fe_2O_4$ powders were prepared by the one-pot solution combustion method. The effect of calcination temperatures (700°C and 800°C) on phase, structure, microstructure and magnetic properties of $SrFe_{12}O_{19}$-x $Ni_{0.6}Zn_{0.4}Fe_2O_4$ (x = 0 wt.%, 10 wt.%, 20 wt.% and 30 wt.%) composites were investigated by x-ray diffractometry, scanning electron microscopy and vibrating sample magnetometry techniques. Strontium hexaferrite and spinel ferrite phases were formed through calcination at 800°C together with some α-Fe_2O_3 phase, while spinel ferrite was mainly crystallized at 700°C. The saturation magnetization slightly increased from 38 emu/g to 42 emu/g with the addition of 10 wt.% of $Ni_{0.6}Zn_{0.4}Fe_2O_4$ and then decreased to 36 emu/g at a calcination temperature of 800°C. The microwave absorption measurements in X-band (8–12 GHz) showed a minimum reflection loss of – 14.5 dB at 9.5 GHz for $SrFe_{12}O_{19}$-10 wt.% $Ni_{0.6}Zn_{0.4}Fe_2O_4$ composite synthesized at 800°C.

Key words: $SrFe_{12}O_{19}/Ni_{0.6}Zn_{0.4}Fe_2O_4$ composite, solution combustion synthesis, calcination temperature, magnetic properties, microwave absorption

INTRODUCTION

In order to minimize the reflection of radar signals from a vehicle, several techniques such as shape design, passive and active cancellation of electromagnetic wave energy, and electromagnetic absorbing materials can be employed. The reduction of radar signal through the shape design may not be preferred and thus the knowledge of microwave absorbing magnetic materials is essential to abate the radar signal. Therefore, magnetic spinel ferrites and hexagonal ferrites have been utilized as absorbing materials, recently. Magnetic spinel and hexagonal ferrites are suitable candidates for microwave absorbing materials to mitigate electromagnetic pollution and interference in wireless communication.[1,2] Magnetic ferries have unique physical and chemical properties such as high resistivity, high resonance frequency, low permittivity, low density, and good chemical stability in comparison with magnetic metals used in microwave absorption.[3] Spinel and hexagonal ferrites show the resonance frequency in megahertz and gigahertz range, respectively, leading to the absorption of a narrow band of electromagnetic waves at microwave frequency.[4] Therefore, soft/hard ferrite composites with enhanced magnetic properties can show higher microwave absorption performance than ferrite materials with single absorbing mechanisms.[5,6]

Soft/hard ferrite composites are gaining great attention due to their superior magnetic properties

---

(Received June 17, 2019; accepted January 3, 2020;

via the exchange-coupling effect between soft and hard magnetic phases.[7–9] The exchange-coupling strongly depends on the exchange stiffness of the interface and microstructural features such as particle size, shape, and distributions of magnetically hard and soft phases which are tunable by the synthesis route.[8,10–12] The simple synthesis route to prepare magnetic composites is the physical mixing of previously synthesized soft and hard magnetic particles, presenting the weak exchange-coupling effect.[13] The optimal exchange-coupling effect can be achieved by in situ chemical synthesis such as precipitation, hydrothermal, thermal decomposition, solution combustion synthesis, etc., due to homogenous mixing of various magnetic phases.[14–16] Among the various wet chemical routes, the solution combustion synthesis (SCS) method shows many advantages such as facile operation, low cost, and being energy-efficient with short reaction time.[17] SCS exploits an exothermic reaction between the oxidants (metal nitrates, metal chlorides, etc.) and a suitable organic fuel (such as citric acid, glycine, urea, etc.).[18] Enough thermal energy released during combustion results in direct synthesis of final products or with further calcination at low temperatures for complicated structures.[19] Phase purity, particle size, and physical properties are thus related to the calcination temperature, leading to the control of the exchange-coupling effect.[20] Several soft/hard ferrite composites such as $Ni_{0.5}Zn_{0.5}Fe_2O_4/SrFe_{12}O_{19}$, $Mn_{0.2}Ni_{0.4}Zn_{0.4}Fe_2O_4/BaFe_{12}O_{19}$, $Ni_{0.5}Zn_{0.5}Fe_2O_4/BaFe_{12}O_{19}$@polyaniline, graphene/$BaFe_{12}O_{19}$-$Ni_{0.8}Zn_{0.2}Fe_2O_4$, etc. were successfully prepared by the SCS method as microwave absorbing materials.[21–24] However, the composites had a large particle size due to the use of high calcination temperatures (> 1000°C).

In this work, phase, microstructure, magnetic, and microwave absorption properties of the $SrFe_{12}O_{19}$ (SFO)-x $Ni_{0.6}Zn_{0.4}Fe_2O_4$ (NZFO) (x = 10 wt.%, 20 wt.%, 30 wt.%) composites were investigated as a function of calcination temperatures (700°C and 800°C). The absence of exchange-coupling interaction between soft and hard magnetic particles was determined from the demagnetization (dM/dH) curves that can be assigned to the low calcination temperature, thru the incomplete formation of ferrites.

EXPERIMENTAL PROCEDURE

The ethylenediaminetetraacetic acid ($C_{10}H_{16}N_2O_8$) as fuel was dissolved in distilled water by adding an ammonia (NH_4OH) solution (25 wt.%) to increase the pH value up to 9. Then, required amounts of $Fe(NO_3)_3{\cdot}9H_2O$, $Sr(NO_3)_2{\cdot}6H_2O$, $Ni(NO_3)_2{\cdot}6H_2O$ and $Zn(NO_3)_2{\cdot}6H_2O$ were simultaneously added in which the total metal nitrates to fuel molar ratio was 1:1. The dark brown homogeneous solution was heated until it transformed into a gel that was ignited with further heating up to 250°C. The as-combusted powders were calcined at 700°C and 800°C for 1 h in air atmosphere.

Powder x-ray diffraction (XRD) method was used to characterize various phases in composites by PANalytical diffractometer (CuKα = 1.54060 Å). The quantitative analysis was performed by Rietveld refining of XRD patterns using MAUD software.

The particle size and shape of the powders were determined by a TESCAN Vega II field emission scanning electron microscopy (SEM). The magnetic properties of composites were measured by a vibrating sample magnetometer (VSM) (Meghnatis Daghigh Kavir Co., Iran) at room temperature.

Complex permittivity (ε_r) and permeability (μ_r) of SFO-x%NZFO composites were measured in X-band (8–12 GHz) by a vector network analyzer in a PNA, Agilent E8364B instrument. The rectangular standard samples (0.4 × 0.9 in^2) were prepared by mixing powders with paraffin in a 6:4 weight ratio.

Reflection loss, RL (dB), of the electromagnetic wave under perpendicular wave incidence at the surface of a single-layer material backed by a metal can be calculated by the following equations on the base of transmission line theory [25]:

$$\mathrm{RL}\,(\mathrm{dB}) = 20\log\left|\frac{Z_{in}/Z_0 - 1}{Z_{in}/Z_0 + 1}\right|, \tag{1}$$

$$Z_{in}/Z_0 = \sqrt{\mu_r/\varepsilon_r}\tanh\left(j(2\pi ft/c)\sqrt{\mu_r\epsilon_r}\right), \tag{2}$$

where μ_r, ε_r, f, t, and c are relative permeability, permittivity, frequency, thickness, and speed of light, respectively.

RESULTS AND DISCUSSION

Figures 1 and 2 show XRD patterns of the SFO powders and SFO-x%NZFO composites calcined at 800°C and 700°C, respectively. The amounts of various phases in the composites are summarized in Table I. About 15 wt.% of impurity α-Fe_2O_3 phase (JCDPS Card No. 00-033-0664) together with the strontium hexaferrite phase (JCDPS Card No. 00-033-1340) was formed following calcination at 800°C. During the combustion reaction, the metal nitrates are thermally decomposed to the corresponding oxides such as SrO and α-Fe_2O_3 which are then reacted at high temperatures to form strontium hexaferrite as follows:[26]

$$SrO + 6Fe_2O_3 \rightarrow SrFe_{12}O_{19}. \tag{3}$$

Therefore, the residual α-Fe_2O_3 phase can be attributed to the low calcination temperature for the completion of the reaction (3). Accordingly, the amount of α-Fe_2O_3 phase increases up to 31 wt.% with the decrease of calcination temperature at 700°C. Moreover, a slight peak shift towards lower

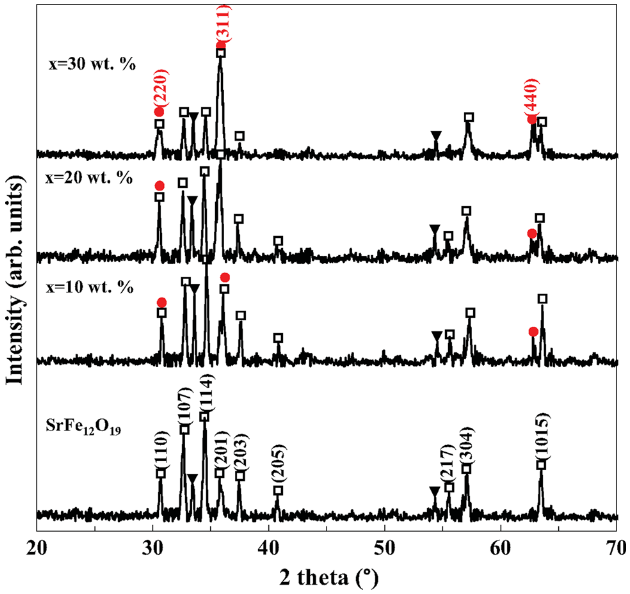

Fig. 1. XRD patterns of the SFO-xNZFO composites calcined at 800°C (□:$SrFe_{12}O_{19}$, ●:$Ni_{0.6}Zn_{0.4}Fe_2O_4$, and ▼:α-Fe_2O_3).

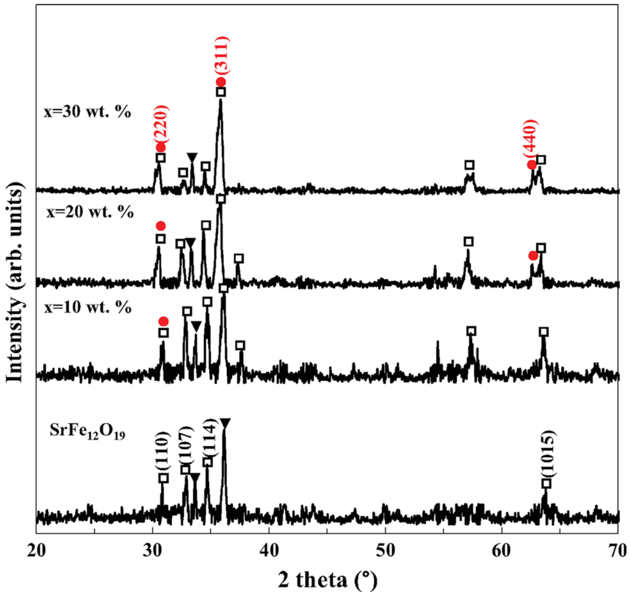

Fig. 2. XRD patterns of the SFO-xNZFO composites calcined at 700°C (□:$SrFe_{12}O_{19}$, ●:$Ni_{0.6}Zn_{0.4}Fe_2O_4$, and ▼:α-Fe_2O_3).

Table I. Phase constituents (wt.%) of the SFO-xNZFO composites as a function of calcination temperature

	SFO	NZFO	α-Fe_2O_3
800°C			
0	85	–	15
10	76	8	16
20	70	17	13
30	56	29	15
700°C			
0	69	–	31
10	76	7	17
20	70	16	14
30	–	–	–

diffraction angles at higher NZFO contents at both calcination temperatures confirms the substitution of nickel and zinc cations in the spinel ferrite structure accompanied by an increase in lattice parameters. M-type strontium hexaferrite ($SrFe_{12}O_{19}$) is made of close-packed oxygen O^{2-} layers in which Fe^{3+} cations are located in octahedral, tetrahedral and trigonal bipyramidal sites, while Sr^{2+} cations enter the oxygen layers, substitutionally. $SrFe_{12}O_{19}$ is also described as a superposition of cubic spinel ($S = Fe_6O_8$) and hexagonal ($R = SrFe_6O_{11}$) blocks built-in RSR^*S^* in which R^* is the corresponding R block turned 180° around the hexagonal *c*-axis.[1] Accordingly, the (110) and (201) reflections of $SrFe_{12}O_{19}$ coincide with (220) and (311) diffraction peaks of spinel ferrites. The hexaferrite reflections are weakened, while the intensity of (220) and (311) spinel peaks increases with the increase of spinel ferrite content, confirming the formation of spinel ferrite together with strontium hexaferrite phase (Table I). Furthermore, the appearance of a distinct (440) spinel peak proves the separate formation of spinel and hexagonal ferrites. The easier formation of spinel ferrite than that of hexaferrite is due to its higher crystal structure symmetry, as confirmed by the appearance of more spinel ferrite phase during calcination at 700°C (Table I). Furthermore, the existence of more α-Fe_2O_3 phase in the composites can be attributed to the slower cation diffusion induced from the higher cation concentrations, postponing the crystallization of hexaferrite and spinel ferrite phases.[27]

SEM micrographs of the SFO powders and SFO-10 wt.%NZFO composites calcined at 800°C and 700°C are compared in Fig. 3. At both calcination temperatures, the powders demonstrate foamy structure with pores being produced through the liberation of a large amount of gasses during combustion while maintaining their structure after calcination at 700°C and 800°C. The porous structure has a higher surface area that is beneficial for the enhancement in microwave absorption of spinel ferrites. SFO powders have platelet particles together with some spherical particles. The formation of platelet particles is due to the hexagonal crystal structure of $SrFe_{12}O_{19}$.[28] The spherical particles can be associated with the α-Fe_2O_3 phase or incomplete formation of strontium hexaferrite at the calcination temperature of 800°C. However, the powders are composed of more spherical particles related to the NZFO phase that are tightly in contact with hexagonal particles. Only spherical particles can be seen in the powders calcined at 700°C, showing the weak crystallization of phases. The particle sizes of nanocomposites synthesized at

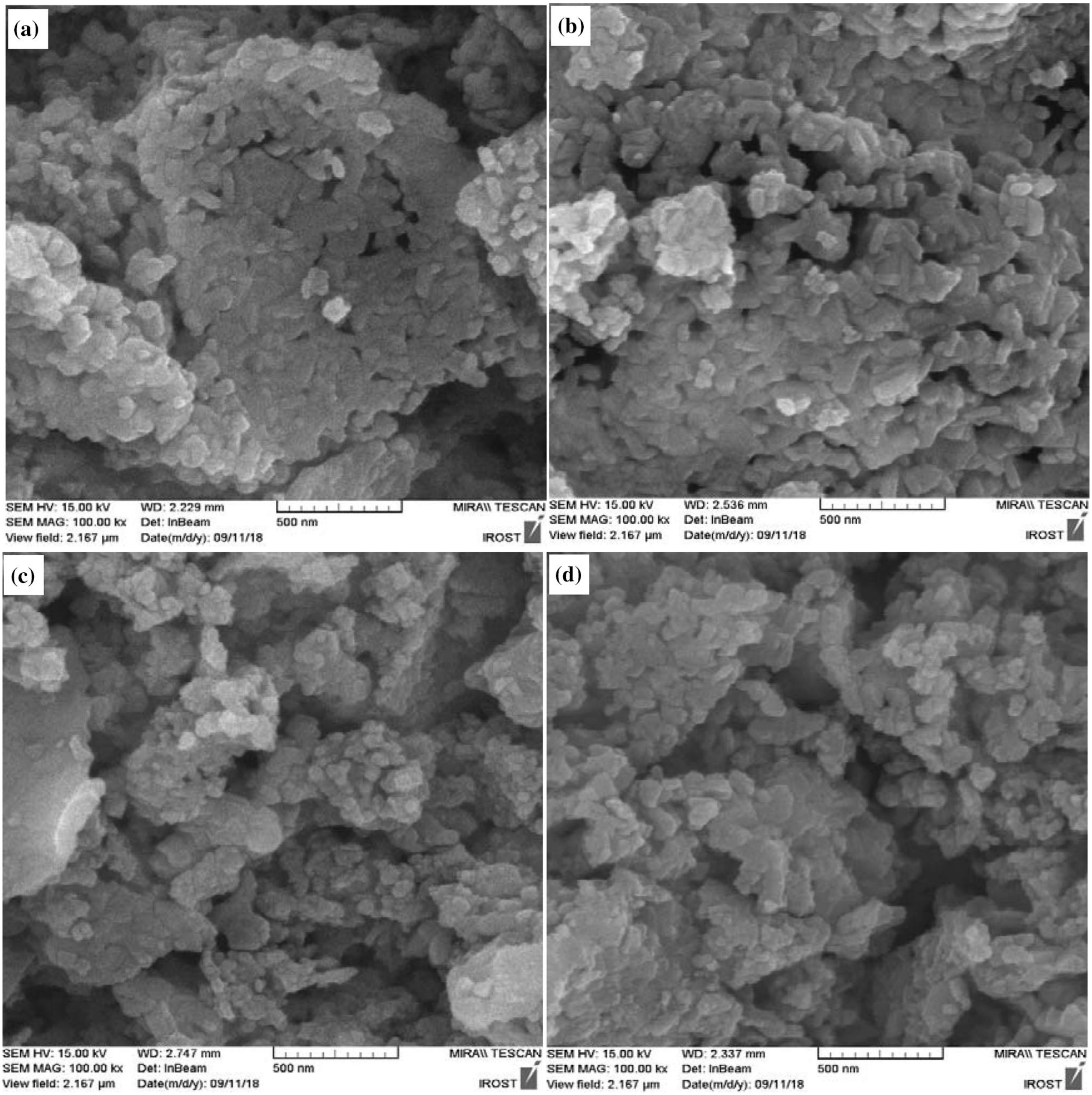

Fig. 3. SEM micrographs of (a) $SrFe_{12}O_{19}$ powders and (b) SFO-10 wt.% NZFO composite calcined at 800°C and (c) $SrFe_{12}O_{19}$ powders and (d) SFO-10 wt.% NZFO composite calcined at 700°C.

700°C and 800°C were measured from SEM micrographs to be about 31.6 nm and 68.2 nm, respectively, and that are much smaller than similar nanocomposites obtained at a higher calcination temperature of (1000°C).[21]

Hysteresis loops of the SFO powders and SFO-x NZFO composites synthesized at 800°C and 700°C are shown in Fig. 4, respectively. In spite of the antiferromagnetic α-Fe_2O_3 phase, SFO powders show a smooth hysteresis loop. However, the demagnetization curve in the second quadrant becomes concave by the addition of NZFO phase.[29] There are three different magnetic interactions between soft/soft, hard/hard, and soft/hard grains in the soft/hard composites. The soft/hard grains can interact via exchange coupling, while the dipolar interactions occur between the soft/soft and hard/hard grains, leading to the double magnetic-phase phenomenon.[30] The knee in hysteresis loops is more intensified by the calcination at 700°C, showing that magnetization reversal cannot be completed in one step.

The switching field distribution (SFD) (dM/dH) can be used for the recognition of exchange coupling

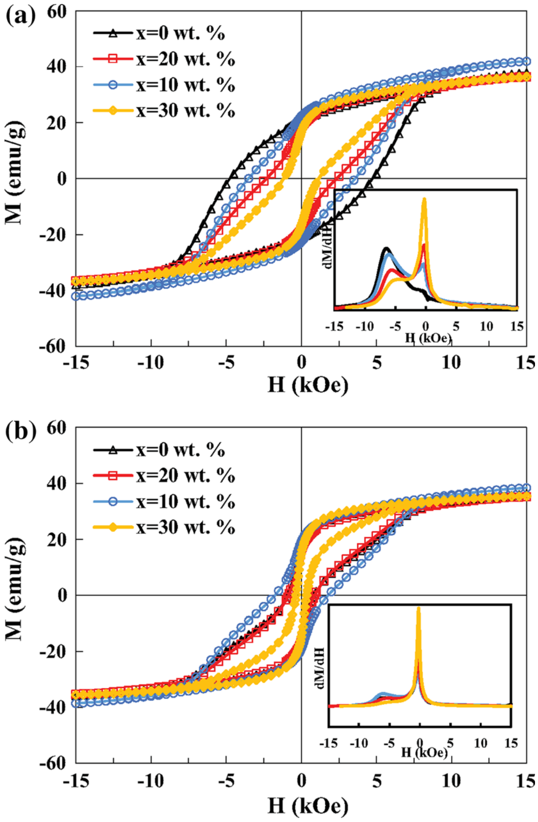

Fig. 4. Hysteresis loops of the SFO-xNZFO composites calcined at (a) 800 and (b) 700°C.

Table II. Magnetic properties of the SFO-xNZFO composites as a function of calcination temperature

	M_s (emu/g)	M_r/M_s	H_c (Oe)
800°C			
0	38	0.55	4736
10	42	0.53	3491
20	36	0.50	2317
30	36	0.46	1166
700°C			
0	36	0.49	852
10	38	0.50	1757
20	35	0.46	849
30	35	0.42	355

interaction.[31] The SFD plots of the powders synthesized at 800°C and 700°C are compared in the inset of Fig. 4. The SFO powders calcined at 800°C exhibit a unimodal inversion-field distribution with a maximum in H_c.[32] However, two peaks at 6500 and 150 Oe corresponded to the hard and soft magnetic phases in composites calcined at 800°C caused by the dipolar interaction. The peak at 150 Oe is intensified by increasing the amount of soft spinel ferrite phase. With the drop of calcination temperature to 700°C, the peak of the hard magnetic phase decreases, showing the weak crystallization of strontium hexaferrite.

The magnetic properties of powders are given in Table II. At 800°C, the saturation magnetization slightly increases from 38 emu/g to 42 emu/g with the addition of 10 wt.% of NZFO, while it decreases up to 36 emu/g at higher amounts of NZFO. Cation distribution between tetrahedral (A) and octahedral (B) sites has a strong effect on the saturation magnetization of spinel ferrites. In NZFO, Zn^{2+}/Ni^{2+} cations and half of the Fe^{3+} cations occupy the B sites while the other half of the iron cations enter into the A sites. The superexchange interaction between cations in A and B sites will impact the saturation magnetization of spinel ferrites based on Neel's theory. Therefore, the increase in saturation magnetization of 10 wt.% NZFO compared to SFO powders could be due to the proper cations distribution between A and B sites. However, at higher amounts of NZFO beyond 10 wt.%, incomplete cation distribution or surface cation disorder lead to the inferior M_s. The lower saturation magnetization at 700°C is due to the incomplete crystallization of ferrites. Furthermore, the squareness (M_r/M_s) values of about 0.5 confirm the non-interacting permanent magnets.[33] With the increase of NZFO phase, the coercivity decreases from 4736 to 1166 Oe and from 852 to 355 Oe at 800°C and 700°C, respectively, due to the effortless formation of reverse domains in soft ferrite phase.[34]

The reflection, propagation, and attenuation of an electromagnetic wave in a material depend on relative permittivity ($\varepsilon_r = \varepsilon_r' - j\varepsilon_r''$) and permeability ($\mu_r = \mu_r' - j\mu_r''$) as microwave properties. The storage capability of magnetic and electric energy is described by real parts (μ_r' and ε_r'), while the imaginary parts (μ_r'' and ε_r'') indicate the loss of magnetic and electric energy, respectively.[35] The complex permittivity and permeability spectra of pure SFO powder and SFO-10 wt.% NZFO composite calcined at 700°C and 800°C are compared in Fig. 5a and b, respectively. The real and imaginary parts of permittivity remain constant in the X band (8–12 GHz). With the addition of the NZFO phase, however, the real part (ε_r') of permittivity decreases from ~ 3.25 to 2.75, irrespective of calcination temperature. The decrease of ε_r' can be attributed to the weak polarization of Fe^{3+}-O^{2-} and M^{2+}-O^{2-} (M = Ba, Ni and Zn) dipoles in spinel ferrites.[36] Furthermore, the dielectric loss (ε_r'') slightly decreases in the presence of the NZFO phase. It is well known that the microwave magnetic lost is due to hysteresis, eddy current, domain wall resonance, and natural ferromagnetic resonance.[37] In the case of a weak applied field, the hysteresis loss is minimal. In this study, the permeability was measured over a narrow frequency range of 8–12 GHz where the domain wall resonance (mainly activated at 1–100 MHz) is reasonably weak to contribute towards magnetic loss. Furthermore, the eddy current is dominated in materials with high

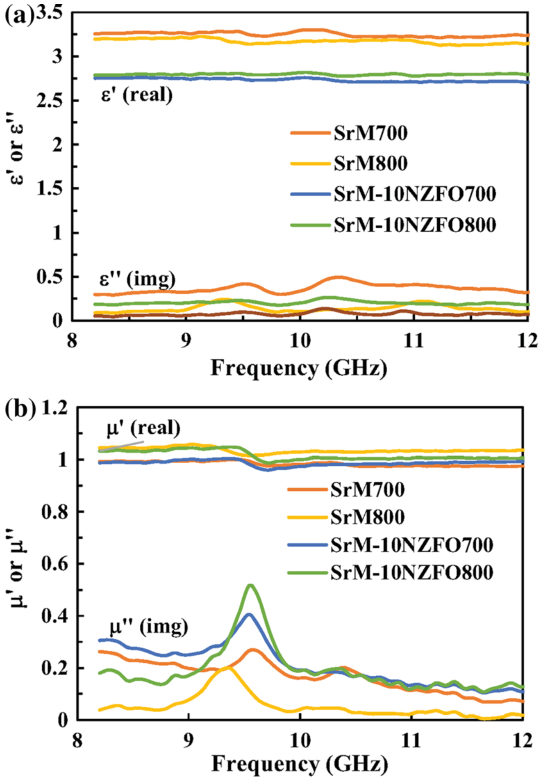

Fig. 5. (a) Relative permittivity and (b) relative permeability spectra of the synthesized powders.

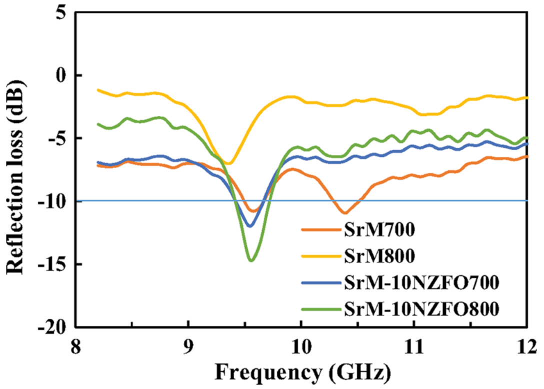

Fig. 6. Reflection loss of the synthesized powders at thickness of 3.5 mm.

conductivity, while in the case of insulating/semiconducting oxides, eddy current loss would not play a major role. Therefore, the imaginary part of permeability shows a dispersion in the range of 9–10 GHz due to the natural ferromagnetic resonance mechanism. While the natural resonance frequency (f_r) of $SrF_{12}O_{19}$ is more than ~ 40 GHz, the decrease of f_r can be attributed to the reduction of anisotropy field caused by weak crystallinity of hexaferrite.[4] The SFO-10 wt.% NZFO powders calcined at 800°C exhibit the highest magnetic loss (μ_r'') due to their highest saturation magnetization.

Figure 6 shows the reflection loss versus frequency at 3.5 mm thickness. The higher reflection loss means the better absorption of electromagnetic waves. The minimum reflection loss of − 14.5 dB at 9.5 GHz with a bandwidth of 0.3 GHz (at − 10 dB) is achieved by SFO-10 wt.% NZFO powders calcined at 800°C. Two problems need to be resolved to obtain low reflection or strong absorption. The first matter is the penetration of incident electromagnetic (EM) waves into the material with the lowest reflection and the other is the absorption of the maximum amount of EM wave. The impedance match between the material and free space ($\sqrt{\mu_r/\varepsilon_r} = 1$) is needed for effective penetration, satisfied by high real permeability μ' and low real permittivity ε'. In the second problem, the absorber material should have high imaginary parts (ε'' and μ'') at microwave frequency.[37] Therefore, the weak absorption performance of the synthesized powders can be due to their low real and imaginary permeability parts caused by the antiferromagnetic α-Fe_2O_3 phase and low crystallinity.

CONCLUSIONS

One-pot solution combustion synthesis method was used to prepare SFO-xNZFO composites at calcination temperatures of 700°C and 800°C. The formation of strontium hexaferrite and spinel ferrite phases was confirmed by the appearance of a (440) peak with intensified (220) and (311) peaks and different morphologies. The saturation magnetization slightly increased from 38 emu/g to 42 emu/g for x = 10 wt.%, while it decreased to 36 emu/g for higher amounts of NZFO phase following calcination at 800°C. The absence of exchange coupling between ferrites led to the knee in the hysteresis loops. The highest magnetic loss (μ_r'') in the X-band frequency resulted in the maximum absorption of − 14.5 dB at 9.5 GHz with a bandwidth of 0.3 GHz for $SrFe_{12}O_{19}$-10 wt.% $Ni_{0.6}Zn_{0.4}Fe_2O_4$ powders calcined at 800°C.

CONFLICTS OF INTEREST

There is no conflict of interest.

REFERENCES

1. A. Goldman, *Modem Ferrite Technology*, 2nd ed. (Pittsburgh: Springer, 2006).
2. K.J. Vinoy and R.M. Jha, *Radar Absorbing Materials*, 1st ed. (New York: Springer, 1996).
3. R. Valenzuela, *Magnetic Ceramics* (Cambridge: Cambridge University Press, 1994).
4. R.C. Pullar, *Prog. Mater. Sci.* 57, 1191 (2012).
5. G.C.P. Leite, E.F. Chagas, R. Pereira, R.J. Prado, A.J. Terezo, M. Alzamora, and E. Baggio-Saitovitch, *J. Magn. Magn. Mater.* 324, 2711 (2012).
6. X. Shen, F. Song, J. Xiang, M. Liu, Y. Zhu, and Y. Wang, *J. Am. Ceram. Soc.* 95, 3863 (2012).
7. M.A. Radmanesh and S.A. Seyyed Ebrahimi, *J. Magn. Magn. Mater.* 324, 3094 (2012).
8. S.M.A. Radmanesh and S.A. Seyyed Ebrahimi, *J. Supercond. Novel Magn.* 26, 2411 (2013).

9. D. Roy and P.S. Anil Kumar, *J. Appl. Phys.* 106, 073902 (2009).
10. V. Sharma, S. Kumari, and B.K. Kuanr, *J. Alloys Compd.* 736, 266 (2018).
11. S.R. Saeedi Afshar, M. Hasheminiasari, and S.M. Masoudpanah, *J. Magn. Magn. Mater.* 466, 1 (2018).
12. P. Jenuš, M. Topole, P. McGuiness, C. Granados-Miralles, M. Stingaciu, and M. Christensen, *Spomenka Kobe Kristina Žužek Rožman* 99, 1927 (2016).
13. H. Nikmanesh, M. Moradi, P. Kameli, and G.H. Bordbar, *J. Electron. Mater.* 46, 5933 (2017).
14. L. Pan, D. Cao, P. Jing, J. Wang, and Q. Liu, *J. Nanoscale Res. Lett.* 10, 131 (2015).
15. C. Granados-Miralles, M. Saura-Múzquiz, H.L. Andersen, A. Quesada, J.V. Ahlburg, A. Dippel, E. Canévet, and M. Christensen, *ACS Appl. Nano Mater.* 1, 3693 (2018).
16. P. Veverka, E. Pollert, K. Závěta, S. Vasseur, and E. Duguet, *Nanotechnology* 19, 215705 (2008).
17. A. Varma, A.S. Mukasyan, A.S. Rogachev, and K.V. Manukyan, *Chem. Rev.* 116, 14493 (2016).
18. H.H. Nersisyan, J.H. Lee, J.-R. Ding, K.-S. Kim, K.V. Manukyan, and A.S. Mukasyan, *Prog. Energy Combust. Sci.* 63, 79 (2017).
19. F. Li, J. Ran, M. Jaroniec, and S.Z. Qiao, *Nanoscale* 7, 17590 (2015).
20. S.M. Masoudpanah and S.A. Seyyed Ebrahimi, *J. Magn. Magn. Mater.* 324, 2239 (2012).
21. Q. Han, X. Meng, and C. Lu, *J. Alloys Compd.* 768, 742 (2018).
22. S. Hazra, B.K. Ghosh, H.R. Joshi, M.K. Patra, R.K. Jani, S.R. Vadera, and N.N. Ghosh, *RSC Adv.* 4, 45715 (2014).
23. X. Meng, Q. Han, Y. Sun, and Y. Liu, *Ceram. Int.* 45, 2504 (2019).
24. Y. Wang, Y. Huang, Q. Wang, Q. He, and M. Zong, *J. Sol. Gel. Sci. Technol.* 67, 344 (2013).
25. Z. Han, D. Li, M. Tong, X. Wei, R. Skomski, W. Liu, Z.D. Zhang, and D.J. Sellmyer, *J. Appl. Phys.* 107, 09A929 (2010).
26. E. Kiani, A.S.H. Rozatian, and M.H. Yousefi, *J. Mater. Sci. Mater. Electron.* 24, 2485 (2013).
27. S. Kanagesan, M. Hashim, S. Jesurani, T. Kalaivani, I. Ismail, and C.S. Ahmod, *J. Mater. Sci. Mater. Electron.* 24, 3881 (2013).
28. S.M. Masoudpanah, S.A. Seyyed Ebrahimi, and C.K. Ong, *J. Magn. Magn. Mater.* 324, 2654 (2012).
29. A. Rahman and R. Jayaganthan, *Surf. Eng.* 33, 810 (2017).
30. N.A. Spaldin, *Magnetic Materials: Fundamentals and Applications* (Cambridge: Cambridge University Press, 2010).
31. F. Liu, Y. Hou, and S. Gao, *Chem. Soc. Rev.* 43, 8098 (2014).
32. Y. Deng, G.P. Zhao, L. Chen, H.W. Zhang, and X.L. Zhou, *J. Magn. Magn. Mater.* 323, 535 (2011).
33. S. Torkian, A. Ghasemi, and R.S. Razavi, *J. Magn. Magn. Mater.* 416, 408 (2016).
34. D. Roy, C. Shivakumara, and P.S. Anil Kumar, *J. Magn. Magn. Mater.* 321, L11 (2009).
35. Z.W. Li, L. Chen, and C.K. Ong, *J. Appl. Phys.* 94, 5918 (2003).
36. M. Jazirehpour and S.A. Seyyed Ebrahimi, *J. Alloys Compd.* 638, 188 (2015).
37. X. Zhao, Z. Zhang, L. Wang, K. Xi, Q. Cao, D. Wang, Y. Yang, and Y. Du, *Sci. Rep.* 3, 3421 (2013).